Chinese Chemical Letters 34 (2023) 108292

Contents lists available at ScienceDirect

Chinese Chemical Letters

journal homepage: www.elsevier.com/locate/cclet

Pt overlayer for direct oxidation of CH_4 to CH_3OH

Haoyu Li[a], Wei Pei[b,*], Xiaowei Yang[a], Si Zhou[a], Jijun Zhao[a]

[a] Key Laboratory of Materials Modification by Laser, Ion and Electron Beams (Dalian University of Technology), Ministry of Education, Dalian 116024, China
[b] College of Physics Science and Technology, Yangzhou University, Yangzhou 225009, China

ARTICLE INFO

Article history:
Received 6 August 2022
Revised 4 February 2023
Accepted 2 March 2023
Available online 4 March 2023

Keywords:
CH_4 conversion
Pt(111) overlayer
d-band center

ABSTRACT

Highly selective conversion of methane (CH_4) to methanol (CH_3OH) is an emerging attractive but challenging process for future development of hydrogen economy, which requires efficient catalysts. Herein, we systematically explore the catalytic properties of Pt(111) overlayer on transition metal oxides (TMOs) for CH_4 conversion by first principles calculations. The Pt(111) monolayer supported by Ce-terminated CeO_2(111) substrate exhibits high activity and selectivity for CH_4 conversion to CH_3OH, with the kinetic barrier of rate-limiting step of 1.05 eV. Intriguingly, the surface activity of Pt overlayer is governed by its d-band center relative to the energy of bonding states of adsorbed molecules, which in turn depends on the number of charge transfer between Pt(111) monolayer and underlying TMOs substrates. These results provide useful insights in the design of metal overlayers as catalysts with high-ultra performance and atomic utilization.

Natural gas has been widely used as a clean energy source in industrial manufactures and daily routine [1,2]. Methane (CH_4) is the main ingredient of natural gas and has harmful effects on the environment due to its strong greenhouse effect [3–5]. Therefore, there is an urgent need for conversion of CH_4 to high-value products or liquid fuels, which is crucial for storage and transportation of CH_4. At present, the catalytic CH_4 conversion is mainly based on thermocatalysis [6,7], photocatalysis [8,9], electrocatalysis and enzymecatalysis [10–15]. Among them, the thermocatalysis approach has been widely used in industry because of its relatively low cost and high efficiency [6,7]. The dissociation of CH_4 molecule is a key step for CH_4 conversion, and one of the most suitable catalysts are group-VIIIB transition metals, especially Pt-based nanoparticles, nanoshells, and single atoms [16,17].

The previous studies have reported that platinum has decent catalytic performances for CH_4 conversion to produce hydrogen [18,19]. Rategarpanah *et al.* demonstrated that the addition of a small amount of Pt to the Ni-Cu nanoalloys supported on $MgO{\cdot}Al_2O_3$ powders can considerably promote the CH_4 activation, in which the CH_4 conversion rate increases from 70% to 80%, and the H_2 formation rate increases from ~1.35 mol g^{-1} min^{-1} to ~1.55 mol g^{-1} min^{-1} [19]. Moreover, Hosseini *et al.* [20] reported that the Fe_2O_3@CeO_2 core-shell structure loaded with Pt nanoparticles achieves about 80% conversion rate in the dry reforming of methane (DRM), leading to the production of CO_x-free (< 2 ppm) H_2 in the oxidation step by steam with a cyclically stable yield (10.8 mmol/g catalyst-oxygen carrier). Comparing with nanoparticles, dispersed Pt single atom or few atoms exhibits outstanding capabilities for CH_4 conversion [21–26]. For instance, Yan *et al.* [22] reported that Pt single atoms supported on Mn_2O_3 owns excellent catalytic activity for CH_4 oxidation with 90% conversion rate at 603 °C. Gao *et al.* [26] showed that Pt single atoms supported on La_2O_3 precursor with carbon species (Pt_1/LP) have improved activity for CH_4 conversion with regard to Pt nanoparticles. When Pt_1/LP was supported on CeO_2 surface obtained by using precipitation method, the CH_4 conversion rate can be further enhanced to 82%.

It is known that single-atom catalysis faces the problem of low density of active sites (<1 wt%) on the substrate, which limits the catalysis of complicated or multi-electron reactions [27]. Atomically thin layers of transition metals combine the advantages of nanoparticle and single-atom catalysts, providing a large number of active sites as well as maximizing the atomic utilization [28]. Furthermore, the synergistic effect between metal overlayers and the underlying substrates can boost the surficial activities [29–32]. So far, Pt overlayers supported on various transition metal oxides (TiO_2, ZrO_2, CeO_2 and so on) have been synthesized in laboratory [33–41]. Yang *et al.* predicted that Pt monolayer on V_2C MXene exhibits high activity for oxygen reduction reaction owing to the strong metal-support interaction [30]. Later, Li *et al.* successfully synthesized Pt nanolayers with a single or double atomic layer thickness on $Mo_2TiC_2T_x$ MXene, which can catalyze non-oxidative

* Corresponding author.
E-mail address: pwei@yzu.edu.cn (W. Pei).

https://doi.org/10.1016/j.cclet.2023.108292
1001-8417/

coupling of CH_4 to ethane/ethylene [42]. These results shed light in the extraordinary catalytic properties of atomically thin Pt overlayers. However, the principles for tuning the activity of Pt overlayers and the role of different substrates await being understood.

Herein we explore the catalytic behavior of Pt monolayer on transition metal oxides TiO_2, ZrO_2 and CeO_2 for CH_4 conversion by first principles calculations. Among them, Pt monolayer supported on metal-terminated CeO_2 enables direct conversion of CH_4 to methanol (CH_3OH) and suppresses coke formation. The surficial activities of Pt monolayer sensitively depend on the type of substrate, which regulates the d-band center of Pt monolayer. The kinetic barrier of reaction is linearly correlated with the energy difference between d-band center of Pt monolayer and bonding states of adsorbed molecules, which serves as a key descriptor for precise design of novel catalysts for liquid fuel storage.

Density functional theory (DFT) calculations were performed by using the Vienna *ab initio* simulation package (VASP) [43], with the projector augmented wave potentials [44], and the generalized gradient approximation parameterized by Perdew, Burke and Ernzerhof (GGA-PBE) for the exchange and correlation functional [45]. The plane wave basis set with an energy cutoff 500 eV was used. The Brillouin zone was sampled by a $3\times3\times1$ Monkhorst-Pack *k*-point mesh. All structures were optimized using a convergence criterion of 10^{-4} eV and 0.02 eV/Å for total energy and force thresholds, respectively. The DFT-D3 dispersion correction scheme of Grimme was adopted to describe the van der Waals interactions in these layered systems [46]. Kinetic barriers and transition states for CH_4 conversion were simulated using the climbing-image nudged elastic band (CI-NEB) method implemented in VASP [47]. An effective Hubbard parameter $U_{eff}=U-J=5$ eV was used for Ce atoms to consider the strong on-site Coulombic interaction of the Ce 4f orbital [48]. The number of charge transfer between Pt monolayer and underlying substrates was evaluated using the Bader charge analysis [49]. The electronic structures were calculated by DS-PAW program [50].

For the growth of Pt nanofilms in the experiment, transition metal oxides have been widely utilized as substrates [34–42]. Here we considered Pt monolayer on the O-terminated rutile $TiO_2(110)$ and metal-terminated cubic $ZrO_2(100)$ surfaces, which have been synthesized in laboratory [35–40]. For the model of Pt on TiO_2 (hereafter noted as Pt/TiO_2), the supercell consists of 4×2 unit cells of rutile $TiO_2(110)$, with lattice vectors of $\boldsymbol{u}=5\mathbf{a_1}-\mathbf{a_2}$ and $\boldsymbol{v}=2\mathbf{a_1}-5\mathbf{a_2}$ for Pt(111) monolayer. For Pt/ZrO_2, we adopted the supercell comprising Pt(111) monolayer ($\boldsymbol{u}=2\mathbf{a_1}+\mathbf{a_2}$ and $\boldsymbol{v}=\mathbf{a_2}$) on 3×4 unit cells of cubic $ZrO_2(110)$. We also considered cubic CeO_2 as a possible substrate, which has been widely used to support nanofilms, nanoparticles and single atoms for catalysis [51,52]. According to the previous experimental characterization, the surface of CeO_2 sensitively depends on the growth condition [53,54]. In the oxidative atmosphere, CeO_2 tends to form the O-terminated surface, while Ce-termination or a mixture of O- and Ce-termination may occur for CeO_2 prepared in the reductive atmosphere [54,55]. Moreover, the $CeO_2(111)$ surface is non-polar perpendicular to the surface, exhibiting outstanding stability and well-defined geometrical structures compared with the other low-index surfaces [55,56]. Therefore, we constructed Pt(111) monolayer on the O-terminated and Ce-terminated $CeO_2(111)$ to explore the substrate effect. The supercell of Pt/CeO_2 includes 3×3 unit cells of Pt(111) monolayer and 4×4 unit cells of $CeO_2(111)$ substrate. The lattice of Pt overlayer is stretched or compressed to match that of the substrate, resulting in lattice mismatch of 0.54%–3.21%. To elucidate the strain effect on the electronic structure and catalytic property of Pt overlayer, we perform test calculations on Pt(111) monolayer by applying a biaxial stretch strain ranging from 0% to 3.5%. The d-band center is lifted by 0.24 eV toward Fermi level and the adsorption energy of CH_3^* species is weakened by 0.08 eV. Therefore, the strain on Pt overlayer induced by substrates may have a minor effect on the catalytic properties.

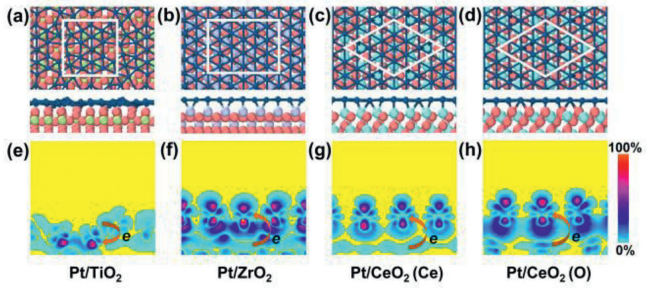

Fig. 1. Geometrical structures of Pt/TMOs hybrid systems. Atomic structures of Pt/TMOs (a-d) and corresponding differential charge density distributions (e-h). White lines labeled the lattice. The Pt, O, Ti, Zr, and Ce atoms are shown by dark blue, pink, green, purple and blue balls, respectively.

Table 1
The key parameters of Pt/TMOs hybrid systems including lattice mismatch (δ), interlayer distance (d), vertical buckling of Pt monolayer (Δd_{Pt}), Pt-Pt bond length ($h_{Pt\text{-}Pt}$), formation energy per Pt atom in Pt monolayer (E_{form}), charge transfer between Pt monolayer and the substrate (CT), the d-band center of Pt monolayer (ε_d).

Structure	Pt/TiO_2	Pt/ZrO_2	Pt/CeO_2 (Ce)	Pt/CeO_2 (O)
δ	2.14%	3.21%	3.29%	3.29%
d (Å)	1.73	2.35	2.58	2.12
Δd_{Pt} (Å)	1.51	0.27	0.42	0.29
$h_{Pt\text{-}Pt}$ (Å)	2.47–2.78	2.64–2.78	2.78–2.98	2.71–2.90
E_{form} (eV)	−1.24	−2.76	−2.04	−0.66
CT (e)	−0.17	0.34	0.33	0.02
ε_d (eV)	−2.54	−2.86	−1.79	−2.14

The structures of Pt overlayer on cubic $ZrO_2(100)$, cubic $CeO_2(111)$ and rutile $TiO_2(110)$ are shown in Fig. 1. The detailed structure parameters are presented in Table 1. The interlayer distance ranges from 1.73 Å to 2.35 Å, which shows the typical covalent interaction between Pt(111) monolayer and underlying TMOs substrates. These interfacial covalent interactions can also be characterized by the differential charge densities, showing the electron accumulation at the interfacial region (Figs. 1e-h). It is worth noting that Pt monolayer grown on TiO_2 exhibits a relatively large deformation with a vertical buckling of 1.51 Å for the Pt monolayer. On the other three substrates, Pt monolayer undergoes slight deformation with small vertical buckling of 0.27∼0.42 Å. The optimized Pt-Pt bond lengths of Pt/TiO_2, Pt/ZrO_2, Pt/CeO_2 (Ce) and Pt/CeO_2 (O) are in the range of 2.47–2.78, 2.64–2.78, 2.78–2.98 and 2.71–2.90 Å, respectively, comparable with that of Pt(111) surface (2.78 Å).

To characterize the thermostabilities of Pt/TMOs hybrid systems, we calculated their formation energy per Pt atom (E_{form}), as follows (Eq. 1):

$$E_{form} = (E_{total} - E_{PtML} - E_{sub})/N \quad (1)$$

where E_{total}, E_{PtML}, and E_{sub} denote the total energy of the Pt/TMOs system, Pt monolayer and TMOs substrate, respectively; N_{Pt} is the number of Pt atoms. As a result, the formation energy of these Pt/TMOs hydride systems range from −0.66 eV/atom to −2.76 eV/atom, signifying the strong bonding interaction between Pt monolayer and underlying TMOs substrates. It is worth noting that the E_{form} of Pt/CeO_2(Ce) is −2.04 eV, which was competitive to or much lower than that of experiment-prepared Pt/TiO_2 ($E_{form}=-1.24$ eV) and Pt/ZrO_2 ($E_{form}=-2.76$ eV). According the Bader charge analysis [49], charge transfer is from Pt monolayer to TiO_2 substrate (0.17 e per Pt atom), whereas Pt monolayer gain electrons from the other substrates (0.02–0.34 e per Pt atom) (Table 1). Figs. 1e-h depicts the two-dimensional charge distribu-

tion between Pt monolayer and substrates. The interfacial charge transfer is correlated to the electronegativity of atoms. The electronegativities of Ti, Zr, Ce, O and Pt are 1.54, 1.33, 1.12, 3.34 and 2.28, respectively. For Pt/ZrO_2 and Pt/CeO_2 (Ce) systems, due to the high electronegativity of Pt compared with Zr and Ce, Pt atoms of Pt/ZrO_2 and Pt/CeO_2 (Ce) gains some electrons (0.34 and 0.33 e per Pt atom) from the underlying Zr and Ce, respectively. For Pt/TiO_2, the electronegativity of O exceeds electronegativity of Pt, and hence each Pt atom loses electrons of 0.17 e. In the Pt/CeO_2 (O) system, due to the electronegativity of Ce is less than electronegativity of Ti, Ce atoms affords more electrons to O atoms, which leads to the charge transfer from O to Pt atoms.

A lot of experimental and theoretical studies have indicated that the Pt-based nanomaterials can achieve a decent chemical activity for CH_4 activation and unique selectivity for yielding CH_3OH product [57,58]. We investigate the catalytic process of CH_4 activation and conversion with H_2O on the Pt/TMOs hybrid systems as well as the bulk-phase Pt(111) surface for reference. According to the previous studies [59], the pathway of CH_4 reaction with H_2O to yield CH_3OH mainly includes three relevant processes (Eqs. 2 and 3):

$$CH_4 \rightarrow CH_3^* + H^* \quad (2)$$

$$H_2O \rightarrow OH^* + H^* \quad (3)$$

$$CH_3^* + OH^* \rightarrow CH_3OH^* \quad (4)$$

where * represents an adsorption site on the catalyst surface. Alternatively, the CH_3^* intermediate can be further dehydrogenated *via* Eq. 5:

$$CH_3^* \rightarrow CH_2^* + H^* \quad (5)$$

which provides the opportunity to form olefin.

Fig. 2 shows the reaction energy (ΔH) for each reaction step, where positive (negative) numbers represent endothermic (exothermic) reaction. For Eq. 2, Pt/TiO_2, Pt/CeO_2 (Ce) and Pt/CeO_2 (O) have reaction energies of −1.26 eV, −0.61 eV and −1.54 eV, respectively. In contrast, CH_4 dehydrogenation is unfavorable on Pt/ZrO_2 with a reaction energy of 1.11 eV. The reaction energies for Eqs. 4 and 5 determine the tendency of CH_3^* to combine with OH^* to form CH_3OH or to be further dehydrogenated. The results show that CH_3^* prefers to react with OH^* to yield CH_3OH product on Pt/TiO_2, Pt/ZrO_2 as well as Pt(111) surface, while Pt/CeO_2 with strong chemical activity can dehydrogenate CH_3^* to CH_2^* intermediate. In contrast to other systems, the reaction energies of two Eqs. 4 and 5 on the Pt/CeO_2 (Ce) system are both close to 0. The kinetic barrier dominates selectivity, as will be discussed later. We examined the reaction Eq. 3 to check whether OH^* can be produced by dissociation of H_2O on these systems.

To further evaluate the catalytic performance of each system, we calculated the kinetic barriers for Eqs. 2–5. Figs. 2a and b show the schematic diagrams of CH_4 dehydrogenation and H_2O dissociation on Pt/CeO_2 (Ce) and Pt/TiO_2, respectively. The values of kinetic barriers are represented by bars in Figs. 2c-f. Fig. 3a shows the complete reaction pathways of Pt/CeO_2 (Ce) and the corresponding adsorption conformation. The detailed information of other systems is shown in Fig. 3b. The transition states of Eqs. 2–5 were represented as TS1, TS2, TS3 and TS4, respectively. The kinetic barriers of Pt/TiO_2 are 1.65, 0.77, 1.63 and 1.25 eV for TS1, TS2, TS3 and TS4, respectively. TS2 has a much smaller kinetic barrier than those of other reactive steps. Too easy decomposition of H_2O may occupy the active sites and leads to inactivation of catalyst. The

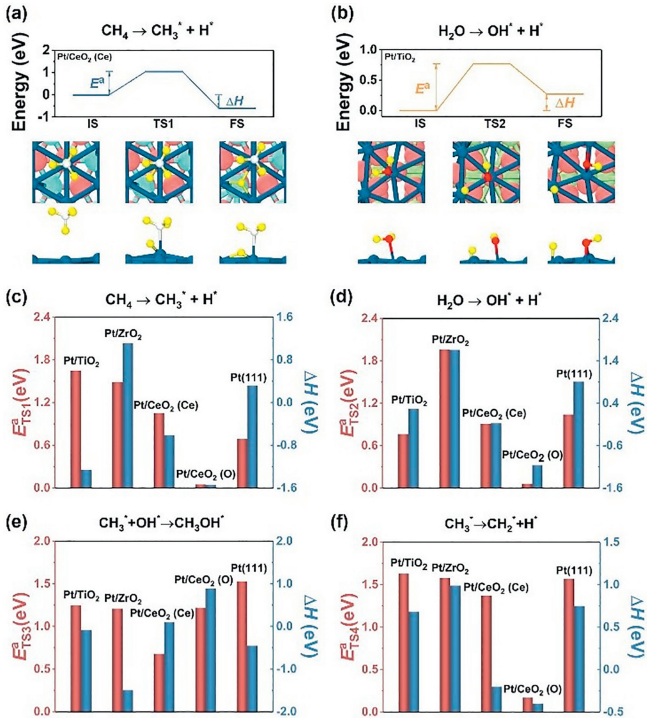

Fig. 2. Kinetic process of CH_4 conversion and H_2O dissociation. Energy diagrams of (a) CH_4 activation and (b) H_2O dissociation on Pt/TMOs. The reaction heat (ΔH), kinetic barriers (E^a), and the corresponding structure configurations are given in insets. Histogram of reaction energies and kinetic barriers for (c) $CH_4 \rightarrow CH_3^* + H^*$, (d) $H_2O \rightarrow OH^* + H^*$, (e) $CH_3^* + OH^* \rightarrow CH_3OH$ and (f) $CH_3^* \rightarrow CH_2^* + H^*$ processes on various Pt/TMOs systems and bulk-phase Pt(111).

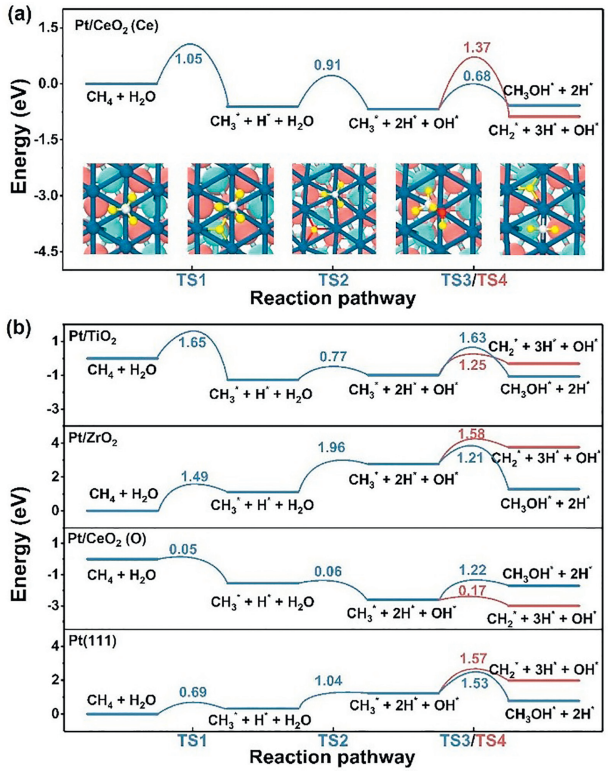

Fig. 3. The reaction pathway of CH_4 conversion. (a) The reaction pathway of CH_4 conversion on Pt/CeO_2 (Ce), and the corresponding structure configurations are given in insets. (b) The reaction pathway of CH_4 conversion on other Pt/TMOs systems and bulk-phase Pt(111) surface. The color number is the kinetic barrier for each reaction step.

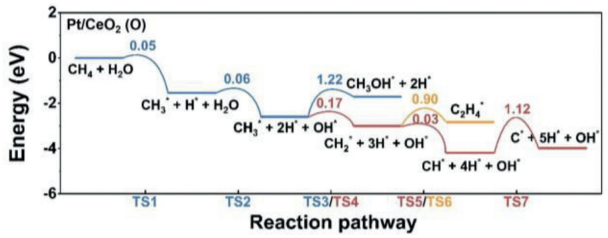

Fig. 4. The further dehydrogenation processes on Pt/CeO_2 (O). The colored number is the kinetic barrier for each reaction step.

kinetic barriers of Pt/ZrO_2 are 1.49, 1.96, 1.21 and 1.58 eV for TS1, TS2, TS3 and TS4, respectively. The high kinetic barrier of H_2O dissociation results in low activity for Pt/ZrO_2, due to the deficiency of OH^* for CH_3OH production. The kinetic barriers of the Pt/CeO_2 (Ce) system are 1.05, 0.91, 0.68 and 1.37 eV for TS1, TS2, TS3 and TS4, respectively. The rate-determining step (RDS) of Pt/CeO_2 (Ce) system is TS1 with kinetic barrier of 1.05 eV, while the RDS of bulk-phase Pt(111) is TS3 with larger kinetic barrier of 1.53 eV. Therefore, the CH_4 to CH_3OH conversion is easier to achieve on Pt/CeO_2 (Ce) than that on bulk Pt. On the other hand, the kinetic TS2, TS3 and TS4, respectively, which indicates that CH_3 dehydrogenation to CH_2^* is more favorable than the formation of CH_3OH. To gain a clear understanding of the product selectivity of Pt/CeO_2 (O), we further consider the following dehydrogenation processes (Eqs. 6 and 7):

$$CH_2^* \rightarrow CH^* + H^* \tag{6}$$

$$CH_2^* + CH_2^* \rightarrow C_2H_4^* \tag{7}$$

$$CH^* \rightarrow C^* + H^* \tag{8}$$

The transition states of Eqs. 6–8 were represented as TS5, TS6 and TS7. As shown in Fig. 4, the kinetic barriers of the above processes on Pt/CeO_2 (O) are 0.03, 0.90 and 1.12 eV for TS5, TS6 and TS7, respectively. The CH_2^* intermediate prefers further dehydrogenation to generate CH^*, rather than the coupling with another CH_2^* to form $C_2H_4^*$. The CH^* species may be further dehydrogenated to produce C^*, which would occupy the active site and poison the catalysts [60]. Therefore, Pt monolayers on various substrates exhibit different catalytic behavior. Pt/CeO_2 (Ce) has higher activity for CH_4 conversion to CH_3OH, while Pt/CeO_2 (O) may be over-reactive and suffer from coke and deactivation.

To further elucidate the substrate effects, we examined the electronic structures of Pt monolayer on various substrates. We calculated the density of states (DOS) for each system after CH_4 adsorption and compared it with the DOS of free gas phase CH_4. Figs. 5a-d show the DOS of Pt/TMOs. The d-band center of the Pt monolayer is calculated using the following equation (Eq. 9) [61]:

$$\varepsilon_d = \frac{\int_{-\infty}^{0} ED(E)\ dE}{\int_{-\infty}^{0} D(E)\ dE} \tag{9}$$

where $D(E)$ is the DOS of the d-band of the Pt monolayer at a given energy E, the integral is taken up to the Fermi level (shifted to zero). The d-band center of the Pt monolayer is indicated by the blue dashed line in Figs. 5a-d. Due to the interfacial charge transfer, the Pt monolayers grown on different substrates have different d-band centers. It is worth noting that the variation of d-band center of Pt monolayer is not only related to the amount of charge transfer, but also depends on the DOS distribution of the substrate. Specifically, the DOS of ZrO_2 is mainly distributed at $-2\sim-7$ eV, which leads to the d-band center of Pt monolayer far away from

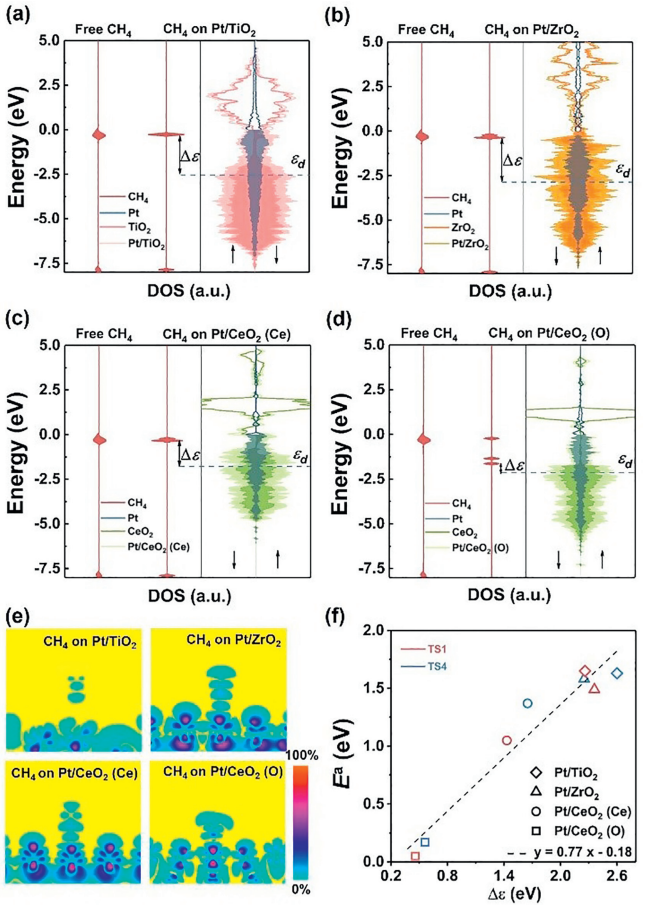

Fig. 5. The orbital interaction of CH_4 adsorbed on Pt/TMOs. (a-d) Local density of states (DOS) of (from left to right) gas-phase and adsorbed CH_4 molecule, and Pt/TMOs. (e) Differential charge density between Pt overlayer and CH_4. (f) The relationship between the kinetic barriers (E^a) and $\Delta\varepsilon$.

the Fermi level (Fig. 5b). The DOS of CeO_2 (O) is mainly distributed at $-1.5\sim-5$ eV, which leads to the d-band center of Pt monolayer closer to the Fermi level (Fig. 5d).

The activity of Pt overlayer is closely related to its d-band center modulated by the presence of substrate. Figs. 5a-d show the energy level of CH_4 upon adsorbing on the Pt overlayer. For Pt/CeO_2 (O), the anti-bonding (σ^*) orbital level of CH_4 exhibits a notable shift to the Fermi level owing to the charge transfer from Pt overlayer to CH_4. The Bader charge analysis shows that CH_4 gains 0.23 e from d orbital of Pt/CeO_2 (O), while only about 0.02 e charge transfer occurred for the other three systems. The injection of electrons increases the polarization of CH_4 molecule, elongating the C-H bond length to 1.09∼1.18 Å and weakening the C-H bond. Fig. 5e depicts the two-dimensional charge distribution between Pt monolayer and CH_4. Fig. 5f displays a linear relationship between the activation energy of C-H bond and the d-band center of Pt overlayer relative to σ^* of CH_4^* ($\Delta\varepsilon$). Roughly speaking, a lower $\Delta\varepsilon$ value indicates more charge transfer from d-band center of Pt overlayer to the anti-bonding orbital of adsorbate, thus resulting in a lower activation energy for C-H bond cleavage in both CH_4 and CH_3^* species. Therefore, the energy difference between d-band center of Pt overlayer and the anti-bonding orbital of adsorbate is a possible descriptor to predict the activation energy of C-H bond, which guides the rational selection of proper substrates to tune the catalytic performance of metal overlayers for certain reactions.

In summary, we investigate the geometrical and electronic structures of Pt monolayer supported on various metal oxide sur-

faces and exploit them for CH_4 conversion based on first principles calculations. Monolayer Pt on Ce-terminated $CeO_2(111)$ surface is a potential catalyst for CH_4 conversion to CH_3OH with high activity and selectivity. The relationship between chemical activity and electronic structure was established for supported Pt monolayer hybrid systems. The reaction occurs more readily with smaller $\Delta\varepsilon$. Moreover, the substrate with more density of states distributed near the Fermi level induces larger changes of the d-band center of Pt monolayer. These computational results provide useful insights for the design of high-efficiency metal overlayers for direct and selective CH_4 conversion.

Declaration of competing interest

The authors declare that they have no known competing financial interests or personal relationships that could have appeared to influence the work reported in this paper.

Acknowledgments

This work was supported by the National Natural Science Foundation of China (Nos. 11974068, 91961204, and 12004065), the Fundamental Research Funds for the Central Universities of China (No. DUT20LAB110), the Liaoning Provincial Natural Science Foundation of China (No. 2019JH3/30100002), and Key Research and Development Project of Liaoning Province (No. 2020JH2/10500003). The authors gratefully acknowledge the computer resources provided by the Supercomputing Center of Dalian University of Technology and Shanghai Supercomputer Center. We gratefully acknowledge HZWTECH for providing computation facilities.

References

[1] Z.R. Chong, S.H.B. Yang, P. Babu, P. Linga, X.S. Li, Appl. Energy 162 (2016) 1633–1652.
[2] S. Faramawy, T. Zaki, A.A.E. Sakr, J. Nat. Gas Sci. Eng. 34 (2016) 34–54.
[3] H. Rodhe, Science 248 (1990) 1217–1219.
[4] D.J. Wuebbles, K. Hayhoe, Earth Sci. Rev. 57 (2002) 177–210.
[5] R.W. Howarth, R. Santoro, A. Ingraffea, Clim. Change 106 (2011) 679–690.
[6] A. Konieczny, K. Mondal, T. Wiltowski, P. Dydo, Int. J. Hydrog. Energy 33 (2008) 264–272.
[7] U.P.M. Ashik, W.M.A. Wan Daud, H.F. Abbas, Renew. Sustain. Energ. Rev. 44 (2015) 221–256.
[8] L. Yuliati, H. Yoshida, Chem. Soc. Rev. 37 (2008) 1592–1602.
[9] X. Li, C. Wang, J. Tang, Nat. Rev. Mater. 937 (2022) 1–16.
[10] N. Spinner, W.E. Mustain, J. Electrochem. Soc. 160 (2013) F1275–F1281.
[11] R.S. Kim, Y. Surendranath, ACS Cent. Sci. 5 (2019) 1179–1186.
[12] J. Jang, K. Shen, C.G. Morales-Guio, Joule 3 (2019) 2589–2593.
[13] M. Merkx, D.A. Kopp, M.H. Sazinsky, et al., Angew. Chem. Int. Ed. 40 (2001) 2782–2807.
[14] R. Balasubramanian, S.M. Smith, S. Rawat, et al., Nature 465 (2010) 115–119.
[15] F.E. Zilly, J.P. Acevedo, W. Augustyniak, Angew. Chem. Int. Ed. 50 (2011) 2720–2724.
[16] R. Zhang, L. Song, Y. Wang, Appl. Surf. Sci. 258 (2012) 7154–7160.
[17] H.B. Ma, T. Sheng, W.S. Yu, et al., ACS Catal. 9 (2019) 10159–10165.
[18] H. Yoshida, K. Hirao, J. Nishimoto, et al., J. Phys. Chem. C 112 (2008) 5542–5551.
[19] A. Rategarpanah, F. Meshkani, Y. Wang, et al., Energy Convers. Manag. 166 (2018) 268–280.
[20] D. Hosseini, P.M. Abdala, F. Donat, et al., Appl. Catal. B: Environ. 258 (2019) 117946.
[21] P. Xie, T. Pu, A. Nie, et al., ACS Catal. 8 (2018) 4044–4048.
[22] D. Yan, J. Chen, H. Jia, Angew. Chem. Int. Ed. 59 (2020) 13562–13567.
[23] S. Ding, H.A. Chen, O. Mekasuwandumrong, et al., Appl. Catal. B: Environ. 281 (2021) 119471.
[24] X. Zhang, Z. Li, W. Pei, et al., ACS Catal. 12 (2022) 3634–3643.
[25] L. Liu, S. Das, Z. Zhang, et al., ACS Appl. Mater. Interfaces 14 (2022) 5363–5375.
[26] Y. Gao, D. Yan, C. Wang, et al., ACS Appl. Nano Mater. 5 (2022) 2688–2698.
[27] H. Jeong, S. Shin, H. Lee, ACS Nano 14 (2020) 14355–14374.
[28] P. Liu, Y. Zhao, R. Qin, et al., Science 352 (2016) 797–800.
[29] S.T. Hunt, M. Milina, A.C. Alba-Rubio, et al., Science 352 (2016) 974–978.
[30] X. Yang, Y. Zhang, Z. Fu, et al., ACS Appl. Mater. Interfaces 12 (2020) 28206–28216.
[31] K. Sasaki, N. Marinkovic, H.S. Isaacs, R.R. Adzic, ACS Catal. 6 (2015) 69–76.
[32] D.V. Esposito, S.T. Hunt, Y.C. Kimmel, J.G. Chen, J. Am. Chem. Soc. 134 (2012) 3025–3033.
[33] Y. Zhou, J.M. Perket, J. Zhou, J. Phys. Chem. C 114 (2010) 11853–11860.
[34] H.P. Steinruck, F. Pesty, L. Zhang, T.E. Madey, Phys. Rev. B 51 (1995) 2427–2439.
[35] S. Bonanni, K. Aït-Mansour, H. Brune, W. Harbich, ACS Catal. 1 (2011) 385–389.
[36] H.B.R. Lee, S.F. Bent, Chem. Mater. 24 (2012) 279–286.
[37] T.Y. Chang, Y. Tanaka, R. Ishikawa, et al., Nano Lett. 14 (2014) 134–138.
[38] S. Roberts, R. Gorte, J. Phys. Chem. 95 (1991) 5600–5604.
[39] V. Pramhaas, M. Roiaz, N. Bosio, et al., ACS Catal. 11 (2021) 208–214.
[40] S. Roberts, R. Gorte, J. Chem. Phys. 93 (1990) 5337–5344.
[41] E. Altman, R. Gorte, J. Catal. 110 (1988) 191–196.
[42] Z. Li, Y. Xiao, P.R. Chowdhury, et al., Nat. Catal. 4 (2021) 882–891.
[43] G. Kresse, J. Furthmüller, Phys. Rev. B 54 (1996) 11169.
[44] G. Kresse, D. Joubert, Phys. Rev. B 59 (1999) 1758.
[45] J.P. Perdew, K. Burke, M. Ernzerhof, Phys. Rev. Lett. 77 (1996) 3865.
[46] S. Grimme, J. Antony, S. Ehrlich, H. Krieg, J. Chem. Phys. 132 (2010) 154104.
[47] G. Henkelman, B.P. Uberuaga, H. Jónsson, J. Chem. Phys. 113 (2000) 9901–9904.
[48] M. Nolan, S.C. Parker, G.W. Watson, Surf. Sci. 595 (2005) 223–232.
[49] G. Henkelman, A. Arnaldsson, H. Jónsson, Comput. Mater. Sci. 36 (2006) 354–360.
[50] P.E. Blöchl, Phys. Rev. B 50 (1994) 17953.
[51] L. Tao, Y.L. Shi, Y.C. Huang, et al., Nano Energy 53 (2018) 604–612.
[52] J. Li, Y. Tang, Y.Y. Ma, et al., ACS Appl. Mater. Interfaces 10 (2018) 38134–38140.
[53] J.H. Li, Z.Q. Liu, D.A. Cullen, et al., ACS Catal. 9 (2019) 11088–11103.
[54] Q.Y. Wang, Y.X. Li, A. Serrano-Lotina, et al., J. Am. Chem. Soc. 143 (2021) 196–205.
[55] J. Vecchietti, P. Pérez-Bailac, P.G. Lustemberg, et al., ACS Catal. 12 (2022) 10482–10498.
[56] Y.Y. Lin, Z.L. Wu, J.G. Wen, K.R. Peoppelmeier, L.D. Marks, Nano Lett. 14 (2014) 191–196.
[57] B. Loenders, Y. Engelmann, A. Bogaerts, et al., J. Phys. Chem. C 125 (2021) 2966–2983.
[58] Y. Cao, Y. Yang, W. Yu, et al., ACS Appl. Mater. Interfaces 14 (2022) 13344–13351.
[59] Z. Liu, E. Huang, I. Orozco, et al., Science 368 (2020) 513–517.
[60] M. Belgued, P. Pareja, A. Amariglio, H. Amariglio, Nature 352 (1991) 789–790.
[61] W. Pei, S. Zhou, J. Zhao, et al., Nano Energy 76 (2020) 105049.